Optics Letters

Spatially resolved common-path high-order harmonic interferometry

M. M. Mang,[1] D. T. Lloyd,[1] P. N. Anderson,[1] D. Treacher,[1] A. S. Wyatt,[2] S. M. Hooker,[1] I. A. Walmsley,[1] and K. O'Keeffe[3,*]

[1]Department of Physics, University of Oxford, Oxford OX1 3PU, UK
[2]Central Laser Facility, STFC Rutherford Appleton Laboratory, Harwell OX11 0QX, UK
[3]College of Science, Department of Physics, Swansea University, Singleton Campus, Swansea SA2 8PP, UK
*Corresponding author: k.okeeffe@swansea.ac.uk

Received 5 July 2018; revised 27 September 2018; accepted 1 October 2018; posted 2 October 2018 (Doc. ID 337968); published 22 October 2018

Spatially resolved interference is observed between high-order harmonics generated in two longitudinally separated gas targets. High-contrast modulations in the intensity of each harmonic order up to the cutoff are observed on-axis in the far field of the source as the separation between the gas targets is increased. For low-order harmonics, additional off-axis modulations are observed, which are attributed to the interference between the contributions from the long quantum trajectories from each gas target. The inherent synchronization of this setup offers the prospect for high-stability metrology of quantum states with ultrafast temporal resolutions.

https://doi.org/10.1364/OL.43.005275

High-order harmonic generation (HHG) has become a versatile source of ultrafast, coherent, extreme ultraviolet radiation [1], enabling high-resolution imaging [2] and the real-time observation of ultrafast dynamics in materials [3]. The fundamental physics of HHG is well described in terms of the semiclassical three-step model [4]: electrons generated via tunnel ionization in the presence of a strong quasi-monochromatic laser field are accelerated back towards their parent ion where they may recombine, resulting in the emission of harmonic photons at energies $E_q = q\hbar\omega$, where q is an odd integer, and ω is the fundamental driving frequency, up to a maximum harmonic energy which depends on the peak laser intensity. For harmonics generated in the plateau region, below the maximum harmonic, there are two predominant paths along which the electron may return to the parent ion with the same kinetic energy. These paths are known as the "short" and "long" quantum trajectories, in reference to the different times an electron spends in the continuum.

In this Letter, we show that by analyzing the spatially resolved harmonic spectrum as a function of the longitudinal separation, Δz, between two HHG sources driven sequentially by the same laser pulse, trajectory-dependent interference can be identified. Evaluating the interference in the $(\omega, r, \Delta z)$ domain, where r is the transverse spatial dimension, two distinct behaviors are observed in the far-field spectrum of the harmonics: high-contrast fringes, well described by simple two-source interference, are observed on-axis for each harmonic order up to the cutoff, whereas off-axis additional interference effects are observed only for harmonics in the plateau region. A model of HHG emission, including propagation from the source to the detector plane, indicates that the observed off-axis interference effects present for plateau harmonics are the result of interference between the components of harmonics generated by electrons moving on long trajectories in one source with the equivalent components generated in the other source; likewise, the observed on-axis interference is dominated by interference between the short trajectory components generated in each source.

In a typical HHG experiment, a Gaussian laser beam is focused into a low-density gas. The on-axis phase of harmonics generated in the focus of the laser beam is given approximately by $\phi_q = q\phi_G + \phi_{\text{atomic}}$, where $\phi_G = -\tan^{-1}(z/z_R)$ is the Gouy phase, z is the longitudinal position in the focus, and z_R is the Rayleigh range. The second term is the atomic dipole phase, which accounts for the phase accumulated by electrons, as they propagate during the HHG process. This is well approximated by $\phi_{\text{atomic}} \approx -\alpha_q^j I(r,z)$, where α_q^j depends on the transit time of the electron in the continuum, and is therefore different for the long ($j = l$) and short ($j = s$) trajectories, and $I(r,z)$ is the spatially varying laser intensity [5]. The phase acquired by the long and short trajectories during the HHG process is crucial for describing phenomena such as the phase matching of HHG [6], the far-field spatial distribution of harmonics [7], and quantum-path interference effects [8].

Interferometry is vital for accessing quantum trajectory information [9] and requires techniques with high temporal resolution and stability. It has recently been demonstrated that the Gouy phase can be used to accurately control the emission time between two longitudinally separated HHG sources with zeptosecond stability [10]. As described in Ref. [10], the phase difference between harmonics generated at two different

longitudinal points in the focus is dominated by ϕ_G, since the intensity and, therefore, ϕ_{atomic}, varies relatively slowly with z through the focus for short trajectories. This results in a delay in the harmonic emission between both sources, which varies linearly with q. This delay was observed experimentally in the form of modulations in the measured intensity of each harmonic as a function of Δz, corresponding to interference in the $(\omega, \Delta z)$ domain.

However, in the interferometer demonstrated by Laban *et al.* [10], no information was presented on the dependence of the interference in the transverse spatial dimension, r. Although the Gouy phase only varies with z, the atomic dipole phase, ϕ_{atomic}, depends on both z and r through its dependence on the laser intensity, $I(r, z)$. In the plateau region of the spectrum, ϕ_{atomic} is also different for the long and short quantum trajectories through α_q^j. Therefore, the transverse variation of ϕ_{atomic} gives rise to a trajectory-dependent divergence of the harmonic radiation, which is also influenced by the transverse phase variation of the driving laser, $\phi_R(r, z)$. It is expected that the far-field distribution from two longitudinally separated HHG sources, therefore, should exhibit interference effects in both r and z, with trajectory-specific interference contained in the r domain. Observing such interference potentially grants experimental access to the phase shifts of the quantum dynamics inherent in harmonic emission, offering new routes for dynamical measurements of electronic and atomic motion.

In our experiments, a Ti:sapphire laser system (KMLabs Dragon) operating at 1 kHz and a center wavelength of 800 nm was used to produce linearly polarized pulses of energy 358 μJ, which were focused into a vacuum chamber using an achromatic lens with a focal length $f = 400$ mm, with a pulse duration on a target of 30 fs. The Rayleigh range of the beam inside the chamber was measured to be approximately 6 mm. Two gas targets were placed along the propagation axis of the Ti:sapphire beam, as illustrated in Fig. 1(a). The first gas target consisted of a thin steel tube with an inner bore diameter of 200 μm, the tip of which was positioned approximately 4 mm before the focus of the laser using a manual x–y–z manipulator. A second gas target, composing a thin-walled nickel tube sealed at one end, which was squeezed to a thickness of approximately 500 μm, was placed after the first target. The thicknesses of both targets were much smaller than the Rayleigh range of the beam such that phase-matching effects within the targets were minimized. Gas exit holes were drilled through the second target *in situ* by the laser beam. This gas target was mounted to a computer-controlled encoded translation stage, allowing Δz to be varied. Prior to any measurements, the second target was scanned through the focus of the laser several times in order to open the exit holes and ensure that there was no clipping of the laser beam, or harmonics, over the scan range. The second gas target was backed with argon gas at a pressure of 6 mbar. Low gas pressures were used to avoid a high gas load in the chamber, as well as to minimize the absorption of harmonics from the first target, as they passed through the second target. The backing pressure of argon in the first gas target was 136 mbar, such that the intensity of the harmonics from this source was the same as that generated in the second target, when both gas targets were at similar positions within the focus. Continuous gas flow through both targets was used throughout the experiment, resulting in a background pressure inside the chamber of 1×10^{-2} mbar. Generated harmonics were recorded using a home-built flat-field spectrometer, with a spectral resolution of 0.04 nm, consisting of an aberration-corrected concave grating (Hitachi: 001-0640) and microchannel plate (MCP) detector. The distance from the focus of the laser to the MCP was 1.46 m. The grating and MCP were housed in a second chamber, separated from the gas-target chamber via a 1 mm diameter aperture, allowing differential pumping of the spectrometer chamber to a background pressure of 1×10^{-6} mbar. The finite size of the MCP meant that a limited number of harmonic orders could be observed in a given scan. The position of the MCP could be moved, while the chamber was under vacuum via a flexible coupling, allowing different regions of the harmonic spectrum to be observed. A typical harmonic spectrum showing harmonic orders $q = 19$ – 23, with gas in both targets, is shown in Fig. 1(b). Each harmonic in the plateau region was observed to consist of an intense on-axis region corresponding to the short trajectory component and an annular structure with higher divergence, which is typical for the long trajectory component [11].

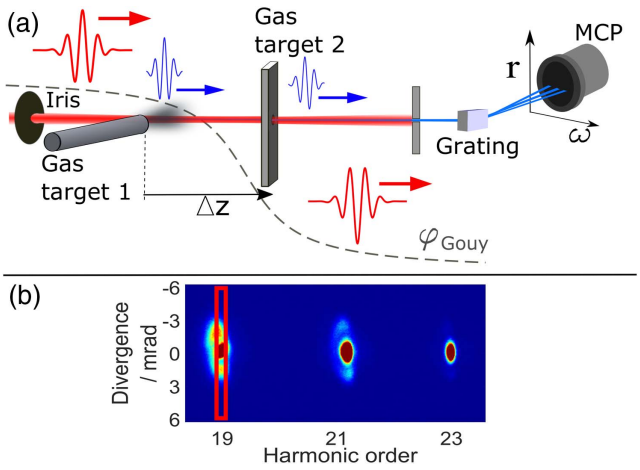

Fig. 1. (a) Experimental setup. The spatio-spectral (r, ω) profile of harmonics generated from two longitudinally separated gas targets is recorded as a function of Δz. The Gouy phase shift across the focus results in a delay between the harmonics generated in each target. (b) Measured (r, ω) profile for harmonics 19–23 with argon in both targets. Interference in the $(\omega, r, \Delta z)$ domain was observed by selecting a spatio-spectral window for each harmonic order and integrating across the spectral domain, as illustrated by the red rectangle surrounding $q = 19$.

An initial longitudinal offset of 0.5 mm was introduced between the gas targets to ensure that their gas plumes did not influence each other at the beginning of a scan. While keeping the position of the first target fixed, Δz was increased by moving the second gas target through the focal region. The harmonic spatio-spectral profile was recorded at each Δz with an exposure time of 0.5 s. Strong modulations in the intensity of each harmonic order were observed as Δz was increased. It was observed that the modulation depth could be optimized by slightly aperturing the laser beam using an iris before the focusing lens, due to small variations imparted to the phase and amplitude of the driving beam [12]. The aperture radius was estimated to be 3.5 mm, corresponding to 90% power transmission. Additional scans were performed with gas in the second target only, as well as with gas in the first target only. The above procedure was repeated for several positions of the MCP, spanning harmonic orders from $q = 15$ to the observed cutoff at $q = 27$.

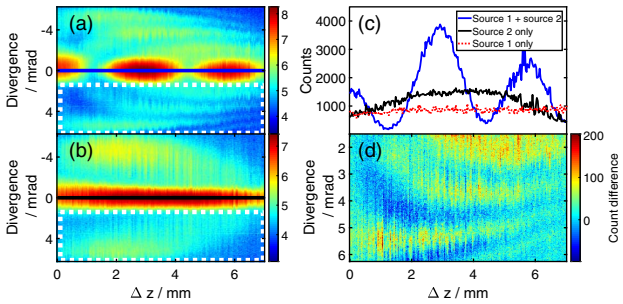

Fig. 2. Spectrally integrated signal for $q = 15$ on a logarithmic scale versus Δz for gas in (a) both sources and (b) the second source only. (c) On-axis harmonic intensity versus Δz for gas in both sources (solid blue line), the second source only (solid black line), and first source only (dotted red line). The horizontal solid lines in (a) and (b) show the position at which the lineouts in (c) were taken. (d) Difference in the signal recorded in (a) and (b) for the off-axis regions indicated by the white dashed rectangles.

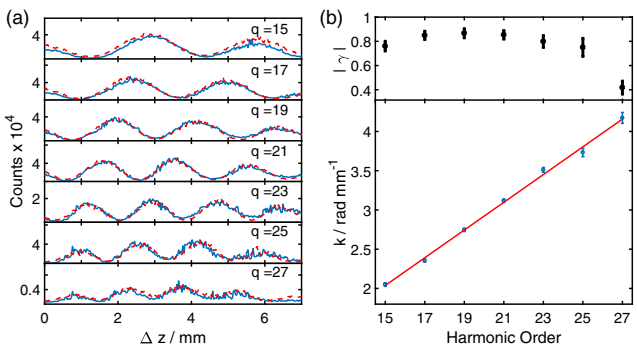

Fig. 3. (a) Measured (solid blue line) and fit to (dashed red line) an on-axis signal versus Δz for harmonic orders 15–27. (b) Upper graph: degree of coherence, $|\gamma|$, of the on-axis interference versus q. Lower graph: measured k-vector of the short trajectory modulations (blue dots) as a function of the harmonic order. The red solid line is a linear fit to data.

The spatial dependence of the interference for each harmonic order as a function of Δz was analyzed by selecting a window in the spatio-spectral profile and integrating across the spectral dimension, as illustrated in Fig. 1(b), allowing the harmonic interference patterns to be analyzed as a function of both Δz and divergence at the detector. Figure 2(a) shows such an interference pattern using a ± 0.3 nm $\times$ ± 6.25 mrad spatio-spectral window centered on harmonic order $q = 15$. Strong on-axis modulations are observed for the central region of the harmonic, as Δz is varied. Figure 2(b) shows the signal within the same spatio-spectral window as a function of Δz with no gas in the first source. In this case, no modulations are present in either the on- or off-axis regions of the harmonic signal, and the intensity and divergence of the off-axis components exhibit only a slow variation with Δz. The on-axis component of the harmonic signal is shown in Fig. 2(c) for gas in both sources (solid blue line), the second source only (solid black line), and the first source only (red dotted line). With gas in both sources, high-contrast fringes are observed across the full range of separations; however, these are completely absent when gas is applied to one gas target only. Fringes are also present at higher divergence angles, as shown in Fig. 2(a); however, these fringes exhibit more complex behavior than those observed on-axis. This is seen clearly in Fig. 2(d), which shows, for the off-axis regions indicated by the dashed boxes, the difference in signal shown in Figs. 2(a) and 2(b).

The on-axis signal for each harmonic order is predominantly due to the contribution from the short trajectory component [11]. To analyze the short trajectory interference component, the average on-axis intensity within a ± 0.3 nm $\times$ ± 0.5 mrad spatio-spectral window centered on the peak of each harmonic was determined as a function of Δz. The blue lines in Fig. 3(a) show the resulting measured interference fringes for different harmonic orders. The measured on-axis intensity of each harmonic order from each source individually was also determined using the same spatio-spectral window. The wavenumber, k_q, degree of coherence, $|\gamma_q|$, and phase offset, δ_q, of the measured on-axis intensity modulation were then extracted for each harmonic order by fitting the measured data to the two-source interference pattern given by the expression

$$I_q(\Delta z) = a_q I_{q1} + I_{q2}(\Delta z) + 2|\gamma_q|\sqrt{a_q I_{q1} I_{q2}(\Delta z)}\cos(k_q \Delta z - \delta_q), \quad (1)$$

where a_q is the transmission of harmonics from the first gas target as they pass through the second target, and I_{q1} and I_{q2} are the measured on-axis intensities of harmonic q from the first and second gas sources, respectively. The values for a_q for propagation through 500 μm of argon at a pressure of 6 mbar were determined using tabulated data [13]. Equation (1) was used to fit the measured two-source interference pattern using the measured I_{q1} and I_{q2}, with k_q, $|\gamma_q|$, and δ_q as fit parameters. The measured interference, as shown by the blue solid lines in Fig. 3(a) and the fit of Eq. (1), shown by the dashed red lines in Fig. 3(a), are in excellent agreement for each harmonic order, across the full range of source separations. In the upper graph of Fig. 3(b), the best fit value of $|\gamma_q|$ retrieved for each harmonic order shows a high degree of coherence between both sources for all harmonics, except at the cutoff. Since the laser peak intensity varies slowly through the focus, and α^s is typically small for short trajectories, ϕ_{atomic} is approximately independent of Δz on-axis. The dominant mechanism for the observed short trajectory interference, therefore, is the Gouy phase contribution to each harmonic order, given by $q\phi_G$ [10]. As a consequence, k_q is expected to vary linearly with q, which is clearly observed in the measured data shown in the lower graph of Fig. 3(b). The average error in k_q across all harmonics measured was 0.04 rad mm^{-1}.

The modulation of the on-axis component of each harmonic order is consistent with a simple two-source interference pattern. However, the measured off-axis interference exhibits more complex behavior, as can be seen in Fig. 2(d). Similar off-axis interference fringes were observed for harmonic orders $q = 15 - 21$. For harmonic orders greater than $q = 21$, no off-axis modulations were observed. Towards the harmonic cutoff, the long and short trajectories merge, such that the distinction between on- and off-axis fringes disappears for the highest harmonic orders.

To better understand the origins of this off-axis interference, an analytical model was developed. The radiating dipole for harmonic q from a source located at position z is defined as

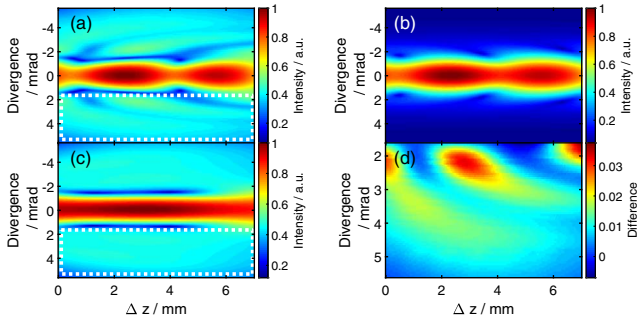

Fig. 4. Simulated spatially resolved interference on a linear scale as a function of Δz for $q = 15$, including (a) long and short trajectory contributions from both sources, (b) short trajectory contributions only from both sources, and (c) long and short trajectory contributions from second source only. (d) Difference signal between the off-axis regions highlighted by the white dashed rectangles shown in (a) and (c).

$$d = \sum_{j=l,s} A_j I(r,z)^{\frac{q_{\text{eff}}}{2}} e^{-i\alpha_q^j I(r,z)} e^{iq(\phi_G + \phi_R(r,z) + \Delta\phi_j)}, \qquad (2)$$

where $A_{l,s}$ is the relative amplitude of the long and short trajectory components, respectively, q_{eff} is a parameter that describes the effective nonlinearity of the interaction, and $\Delta\phi_j$ accounts for the relative phase between the long and short trajectories [11]. The harmonic field was calculated as a function of r for each longitudinal position in the focal region. Since cylindrical symmetry is assumed, and the detector is in the far field, the Hankel transform [14] was used to propagate the harmonic field from each longitudinal position about the focus to the detector, where the resultant interference patterns were calculated. The amplitude and phase of the focused, apertured driving beam were calculated using Lommel functions [12].

The results of simulations for $q = 15$ are shown in Fig. 4. For these simulations, an input driving Gaussian beam with radius 4.5 mm was apertured with a 3.5 mm radius iris, reflecting the experimental conditions. Values for $\Delta\phi_s$ and $\Delta\phi_l$ were chosen to be 0 and $\pi/2$, respectively, based on the mean phase difference between the long and short trajectories in the three-step model, and q_{eff} was taken to be 6, consistent with literature values [15]. The values for α_s and α_l were estimated by calculating the classical action of the electron in the driving field, as described in Ref. [11]. The peak intensity of the laser was estimated to be 1.38×10^{14} W cm^{-2}, based on the observed cutoff at $q = 27$, resulting in values for α_s and α_l of 1.1×10^{14} cm^2 W^{-1} and 23×10^{14} cm^2 W^{-1}, respectively, which are consistent with those reported in the literature [15]. Figure 4(a) shows the calculated spatially resolved interference for $q = 15$ as a function of Δz, including the contributions from both the long and short trajectories. Equal weighting ($A_l = A_s = 1$) was chosen to clearly highlight the effect of the long trajectory contributions. The main features observed experimentally in Fig. 2(a) are reproduced in the simulation. High-contrast modulations are observed on-axis over the full range of Δz, while more complex modulations are observed off-axis. Figure 4(b) shows the calculated interference as a function of Δz, including only the contribution from the short trajectory from each gas target ($A_l = 0$ and $A_s = 1$). In this case, the on-axis interference remains unchanged, while the off-axis interference is no longer present, indicating that the experimentally observed off-axis interference is the result of interference between the long trajectory components from each source. The calculated spatially resolved signal from the second source only, including both trajectories, is shown in Fig. 4(c). The difference signal between the simulated off-axis regions contained within the white dashed rectangles in Figs. 4(a) and 4(c) is shown in Fig. 4(d). Qualitative agreement is observed with the measured difference signal shown in Fig. 2(d).

In conclusion, spatially resolved interference in a common-path extreme ultraviolet interferometer has been observed for the first time to the best of our knowledge. In spite of the sensitivity of long trajectory emission to laser intensity variations, interference can still be observed between long trajectory components from successive sources due to the inherent synchronization and stability of this geometry. These results demonstrate that spatially resolved inline extreme ultraviolet interferometry can be used to observe quantum-path-dependent interference, potentially offering a new approach for probing fundamental ultrafast processes, such as tunnel ionization [16], as well as the characterization of the dispersive properties of materials transparent at extreme ultraviolet wavelengths.

Funding. Engineering and Physical Sciences Research Council (EPSRC) (EP/L015137/1, EP/N029313/1).

REFERENCES

1. F. Krausz and M. Ivanov, Rev. Mod. Phys. **81**, 163 (2009).
2. S. Witte, V. T. Tenner, D. W. Noom, and K. S. Eikema, Light Sci. Appl. **3**, e163 (2014).
3. J. C. Petersen, S. Kaiser, N. Dean, A. Simoncig, H. Y. Liu, A. L. Cavalieri, C. Cacho, I. C. E. Turcu, E. Springate, F. Frassetto, L. Poletto, S. S. Dhesi, H. Berger, and A. Cavalleri, Phys. Rev. Lett. **107**, 177402 (2011).
4. P. B. Corkum, Phys. Rev. Lett. **71**, 1994 (1993).
5. M. Lewenstein, P. Balcou, M. Y. Ivanov, A. L'Huillier, and P. B. Corkum, Phys. Rev. A **49**, 2117 (1994).
6. P. Balcou, P. Salières, A. L'Huillier, and M. Lewenstein, Phys. Rev. A **55**, 3204 (1997).
7. M. Kretschmar, C. Hernández-García, D. S. Steingrube, L. Plaja, U. Morgner, and M. Kovačev, Phys. Rev. A **88**, 013805 (2013).
8. A. Zaïr, M. Holler, A. Guandalini, F. Schapper, J. Biegert, L. Gallmann, U. Keller, A. S. Wyatt, A. Monmayrant, I. A. Walmsley, E. Cormier, T. Auguste, J. P. Caumes, and P. Salières, Phys. Rev. Lett. **100**, 143902 (2008).
9. M. Bellini, C. Lyngå, A. Tozzi, M. B. Gaarde, T. W. Hänsch, A. L'Huillier, and C.-G. Wahlström, Phys. Rev. Lett. **81**, 297 (1998).
10. D. E. Laban, A. J. Palmer, W. C. Wallace, N. S. Gaffney, R. P. M. J. W. Notermans, T. T. J. Clevis, M. G. Pullen, D. Jiang, H. M. Quiney, I. V. Litvinyuk, D. Kielpinski, and R. T. Sang, Phys. Rev. Lett. **109**, 263902 (2012).
11. F. Catoire, A. Ferré, O. Hort, A. Dubrouil, L. Quintard, D. Descamps, S. Petit, F. Burgy, E. Mével, Y. Mairesse, and E. Constant, Phys. Rev. A **94**, 063401 (2016).
12. Z. L. Horváth and Z. Bor, Opt. Commun. **222**, 51 (2003).
13. B. Henke, E. Gullikson, and J. Davis, At. Data Nucl. Data Tables **54**, 181 (1993).
14. L. Yu, M. Huang, M. Chen, W. Chen, W. Huang, and Z. Zhu, Opt. Lett. **23**, 409 (1998).
15. K. Varjú, Y. Mairesse, B. Carré, M. B. Gaarde, P. Johnsson, S. Kazamias, R. López-Martens, J. Mauritsson, K. J. Schafer, P. Balcou, A. L'Huillier, and P. Salières, J. Modern Opt. **52**, 379 (2005).
16. X. Zhou, R. Lock, W. Li, N. Wagner, M. M. Murnane, and H. C. Kapteyn, Phys. Rev. Lett. **100**, 073902 (2008).